

# GEONET: A NEURAL OPERATOR FOR LEARNING THE WASSERSTEIN GEODESIC

**Andrew Gracyk**

Department of Statistics  
University of Illinois at Urbana-Champaign  
agracyk2@illinois.edu

**Xiaohui Chen**

Department of Mathematics  
University of Southern California  
xiaohuic@usc.edu

## ABSTRACT

Optimal transport (OT) offers a versatile framework to compare complex data distributions in a geometrically meaningful way. Traditional methods for computing the Wasserstein distance and geodesic between probability measures require mesh-dependent domain discretization and suffer from the curse-of-dimensionality. We present *GeONet*, a mesh-invariant deep neural operator network that learns the non-linear mapping from the input pair of initial and terminal distributions to the Wasserstein geodesic connecting the two endpoint distributions. In the offline training stage, GeONet learns the saddle point optimality conditions for the dynamic formulation of the OT problem in the primal and dual spaces that are characterized by a coupled PDE system. The subsequent inference stage is instantaneous and can be deployed for real-time predictions in the online learning setting. We demonstrate that GeONet achieves comparable testing accuracy to the standard OT solvers on simulation examples and the MNIST dataset with considerably reduced inference-stage computational cost by orders of magnitude.

## 1 INTRODUCTION

Recent years have seen tremendous progress in statistical and computational optimal transport (OT) as a lens to explore machine learning problems. One prominent example is to use the Wasserstein distance to compare data distributions in a geometrically meaningful way, which has found various applications, such as in generative models (Arjovsky et al., 2017), domain adaptation (Courty et al., 2017) and computational geometry (Solomon et al., 2015). Computing the optimal coupling and the optimal transport map (if it exists) can be expressed in a fluid dynamics formulation with the minimum kinetic energy (Benamou and Brenier, 2000). Such dynamical formulation defines geodesics in the Wasserstein space of probability measures, thus providing richer information for interpolating between data distributions that can be used to design efficient sampling methods from high-dimensional distributions (Finlay et al., 2020). Moreover, the Wasserstein geodesic is also closely related to the optimal control theory (Chen et al., 2021), which has applications in robotics and control systems (Krishnan and Martínez, 2018; Inoue et al., 2021).

Traditional methods for numerically computing the Wasserstein distance and geodesic require domain discretization that is often mesh-dependent (i.e., on regular grids or triangulated domains). Classical solvers such as Hungarian method (Kuhn, 1955), the auction algorithm (Bertsekas and Castanon, 1989), and transportation simplex (Luenberger and Ye, 2015), suffer from the curse-of-dimensionality and scale poorly for even moderately mesh-sized problems (Klatt et al., 2020; Genevay et al., 2016; Benamou and Brenier, 2000). Entropic regularized OT (Cuturi, 2013) and the Sinkhorn algorithm (Sinkhorn, 1964) have been shown to efficiently approximate the OT solutions at low computational cost, handling high-dimensional distributions (Benamou et al., 2015); however, high accuracy is computationally obstructed with a small regularization parameter (Altschuler et al., 2017; Dvurechensky et al., 2018). Recently, a machine learning method to compute the Wasserstein geodesic for a *given* input pair of probability measures has been considered in (Liu et al., 2021).

A major challenge of using the OT-based techniques is that one needs to recompute the Wasserstein distance and geodesic for new input pair of probability measures. Thus, issues of scalability on large-scale datasets and suitability in the online learning setting are serious concerns for modern

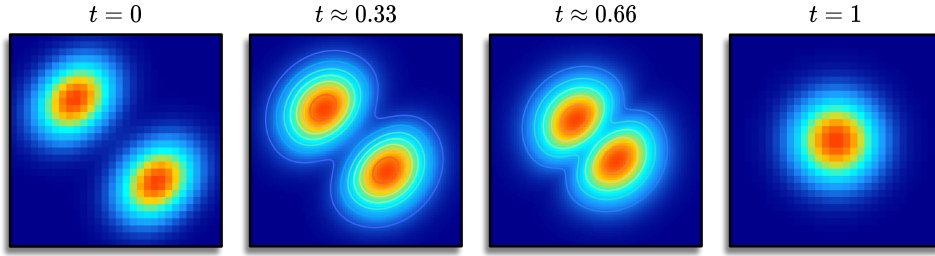


Figure 1: A geodesic at different spatial resolutions. Low-resolution inputs can be adapted into high-resolution geodesics (i.e., super-resolution) with our output mesh-invariant GeONet method.

machine learning, computer graphics, and natural language processing tasks (Genevay et al., 2016; Solomon et al., 2015; Kusner et al., 2015). This motivates us to tackle the problem of learning the Wasserstein geodesic from an *operator learning* perspective.

There is a recent line of work on learning neural operators for solving general differential equations or discovering equations from data, including DeepONet (Lu et al., 2021), Fourier Neural Operators (Li et al., 2020b), and physics-informed neural networks/operators (PINNs) (Raissi et al., 2019) and PINOs (Li et al., 2021). Those methods are mesh-independent, data-driven, and designed to accommodate specific physical laws governed by certain partial differential equations (PDEs).

**Our contributions.** In this paper, we propose a deep neural operator learning framework *GeONet* for the Wasserstein geodesic. Our method is based on learning the optimality conditions in the dynamic formulation of the OT problem, which is characterized by a coupled PDE system in the primal and dual spaces. Our main idea is to recast the learning problem of the Wasserstein geodesic from training data into an operator learning problem for the solution of the PDEs corresponding to the primal and dual OT dynamics. Our method can learn the highly non-linear Wasserstein geodesic operator from a wide collection of training distributions. GeONet is also suitable for zero-shot super-resolution applications on images, i.e., it is trained on lower resolution and predicts at higher resolution without seeing any higher resolution data (Shocher et al., 2018). See Figure 1 for an example of the predicted higher-resolution Wasserstein geodesic connecting two lower-resolution Gaussian mixture distributions by GeONet.

Surprisingly, the training of our GeONet does not require the true geodesic data for connecting the two endpoint distributions. Instead, it only requires the training data as boundary pairs of initial and terminal distributions. The reason that GeONet needs much less input data is because its training process is implicitly informed by the OT dynamics such that the continuity equation in the primal space and Hamilton-Jacobi equation in the dual space must be simultaneously satisfied to ensure zero duality gap. Since the geodesic data are typically difficult to obtain without resorting to some traditional numerical solvers, the *amortized inference* nature of GeONet, where inference on related training pairs can be reused (Gershman and Goodman, 2014), has substantial computational advantage over standard computational OT methods and machine learning methods for computing the geodesic designed for single input pair of distributions (Peyré and Cuturi, 2019; Liu et al., 2021).

Table 1: Comparison of our method GeONet with other existing neural operators and networks for learning dynamics from data. PINN can be found in (Raissi et al., 2019) and the machine learning based minimax method can be found in (Liu et al., 2021). We abbreviate neural operator as NO. We remark we do not check NO for satisfying the PDEs, but the true data is approximated, which do indeed satisfy the PDEs.

Method characteristic	Classical NO	PINNs	Minimax	GeONet (Ours)
no need for retraining for new input	✓			✓
satisfies the associated PDEs		✓	✓	✓
does not require known geodesic data		✓	✓	✓
output mesh independence	✓	✓	✓	✓

Once GeONet training is complete, the inference stage for predicting the geodesic connecting new initial and terminal data distributions requires only a forward pass of the network, and thus it can be performed in real time. In contrast, standard OT methods re-compute the Wasserstein distance and geodesic for each new input distribution pair. This is an appealing feature of amortized inference to use a pre-trained GeONet for fast geodesic computation or fine-tuning on a large number of future data distributions. Detailed comparison between our proposed method GeONet with other existing neural operators and networks for learning dynamics from data can be found in Table 1.

The rest of the paper is organized as follows. In Section 2, we review some background on static and dynamic formulations for the OT problem, as well as on the neural operator learning framework. In Section 3, we present the proposed GeONet method. In Section 4, we report the numeric performance on a synthetic experiment and a real image dataset.

## 2 BACKGROUND

### 2.1 OPTIMAL TRANSPORT PROBLEM: STATIC AND DYNAMIC FORMULATIONS

The optimal mass transportation problem, first considered by the French engineer Gaspard Monge, is to find an optimal map  $T^*$  for transporting a source distribution  $\mu_0$  to a target distribution  $\mu_1$  that minimizes some cost function  $c : \mathbb{R}^d \times \mathbb{R}^d \rightarrow \mathbb{R}$ :

$$\min_{T: \mathbb{R}^d \rightarrow \mathbb{R}^d} \left\{ \int_{\mathbb{R}^d} c(x, T(x)) d\mu_0(x) : T_{\#}\mu_0 = \mu_1 \right\}, \quad (1)$$

where  $T_{\#}\mu$  denotes the pushforward measure defined by  $(T_{\#}\mu)(B) = \mu(T^{-1}(B))$  for measurable subset  $B \subset \mathbb{R}^d$ . In this paper, we focus on the quadratic cost  $c(x, y) = \frac{1}{2}\|x - y\|_2^2$ . The Monge problem (1) induces a metric, known as the *Wasserstein distance*, on the space  $\mathcal{P}_2(\mathbb{R}^d)$  of probability measures on  $\mathbb{R}^d$  with finite second moments. In particular, the 2-Wasserstein distance can be expressed in the relaxed Kantorovich form:

$$W_2^2(\mu_0, \mu_1) := \min_{\gamma \in \Gamma(\mu_0, \mu_1)} \left\{ \int_{\mathbb{R}^d \times \mathbb{R}^d} \|x - y\|_2^2 d\gamma(x, y) \right\}, \quad (2)$$

where minimization over  $\gamma$  runs over all possible couplings  $\Gamma(\mu_0, \mu_1)$  with marginal distributions  $\mu_0$  and  $\mu_1$ . Problem (2) has the dual form (cf. Villani (2003))

$$\frac{1}{2}W_2^2(\mu_0, \mu_1) = \sup_{\varphi \in L^1(\mu_0), \psi \in L^1(\mu_1)} \left\{ \int_{\mathbb{R}^d} \varphi d\mu_0 + \int_{\mathbb{R}^d} \psi d\mu_1 : \varphi(x) + \psi(y) \leq \frac{\|x - y\|_2^2}{2} \right\}. \quad (3)$$

Problems (1) and (2) are both referred as the *static OT* problem, which has close connection to fluid dynamics. Specifically, the Benamou-Brenier dynamic formulation (Benamou and Brenier, 2000) expresses the Wasserstein distance as a minimal kinetic energy flow problem:

$$\begin{aligned} \frac{1}{2}W_2^2(\mu_0, \mu_1) &= \min_{(\mu, \mathbf{v})} \int_0^1 \int_{\mathbb{R}^d} \frac{1}{2} \|\mathbf{v}(x, t)\|_2^2 \mu(x, t) dx dt \\ &\text{subject to } \partial_t \mu + \operatorname{div}(\mu \mathbf{v}) = 0, \quad \mu(\cdot, 0) = \mu_0, \quad \mu(\cdot, 1) = \mu_1, \end{aligned} \quad (4)$$

where  $\mu_t := \mu(\cdot, t)$  is the probability density flow at time  $t$  satisfying the continuity equation (CE) constraint  $\partial_t \mu + \operatorname{div}(\mu \mathbf{v}) = 0$  that ensures the conservation of unit mass along the flow  $(\mu_t)_{t \in [0, 1]}$ . To solve (4), we apply the Lagrange multiplier method to find the saddle point in the primal and dual variables. In particular, for any flow  $\mu_t$  initializing from  $\mu_0$  and terminating at  $\mu_1$ , the Lagrangian function for (4) can be written as

$$\mathcal{L}(\mu, \mathbf{v}, u) = \int_0^1 \int_{\mathbb{R}^d} \left[ \frac{1}{2} \|\mathbf{v}\|_2^2 \mu + (\partial_t \mu + \operatorname{div}(\mu \mathbf{v})) u \right] dx dt, \quad (5)$$

where  $u := u(x, t)$  is the dual variable for the continuity equation. Using integration-by-parts under suitable decay condition for  $\|x\|_2 \rightarrow \infty$ , we find that the optimal dual variable  $u^*$  satisfies the Hamilton-Jacobi (HJ) equation for the dynamic OT problem

$$\partial_t u + \frac{1}{2} \|\nabla u\|_2^2 = 0, \quad (6)$$

and the optimal velocity vector field is given by  $\mathbf{v}^*(x, t) = \nabla u^*(x, t)$ . Hence, we obtained that the Karush–Kuhn–Tucker (KKT) optimality conditions for (5) are solution  $(\mu^*, u^*)$  to the following system of PDEs:

$$\begin{cases} \partial_t \mu + \operatorname{div}(\mu \nabla u) = 0, & \partial_t u + \frac{1}{2} \|\nabla u\|_2^2 = 0, \\ \mu(\cdot, 0) = \mu_0, & \mu(\cdot, 1) = \mu_1. \end{cases} \quad (7)$$

In addition, solution to the Hamilton-Jacobi equation (6) can be viewed as an interpolation  $u(x, t)$  of the Kantorovich potential between the initial and terminal distributions in the sense that  $u^*(x, 1) = \psi^*(x)$  and  $u^*(x, 0) = -\varphi^*(x)$  (both up to some additive constants), where  $\psi^*$  and  $\varphi^*$  are the optimal Kantorovich potentials for solving the static dual OT problem (3). A detailed derivation of the primal-dual optimality conditions for the dynamical OT formulation is provided in Appendix B.

## 2.2 LEARNING NEURAL OPERATORS

A neural operator generalizes a neural network that learns a mapping  $\Gamma^\dagger : \mathcal{A} \rightarrow \mathcal{U}$  between infinite-dimensional function spaces  $\mathcal{A}$  and  $\mathcal{U}$  (Kovachki et al., 2021; Li et al., 2020a). Typically,  $\mathcal{A}$  and  $\mathcal{U}$  contain functions defined over a space-time domain  $\Omega \times [0, T]$ , where  $\Omega$  is taken as a subset of  $\mathbb{R}^d$ , and the mapping of interest  $\Gamma^\dagger$  is implicitly defined through certain differential operator. For example, the physics informed neural network (PINN) (Raissi et al., 2019) aims to use a neural network to find a solution to the PDE

$$\partial_t u + \mathcal{D}[u] = 0, \quad (8)$$

given the boundary data  $u(\cdot, 0) = u_0$  and  $u(\cdot, T) = u_T$ , where  $\mathcal{D} := \mathcal{D}(a)$  denotes a non-linear differential operator in space that may depend on the input function  $a \in \mathcal{A}$ . Different from the classical neural network learning paradigm that is purely data-driven, a PINN has less input data (i.e., some randomly sampled data points from the solution  $u = \Gamma^\dagger(a)$  and the boundary conditions) since the solution operator  $\Gamma^\dagger$  has to obeys the induced physical laws governed by (8). Even though the PINN is mesh-independent, it only learns the solution for a *single* instance of the input function  $a$  in the PDE (8). In order to learn the dynamical behavior of the inverse problem  $\Gamma^\dagger : \mathcal{A} \rightarrow \mathcal{U}$  for an entire family of  $\mathcal{A}$ , we consider the operator learning perspective.

The idea of using neural networks to approximate any non-linear continuous operator stems from the universal approximation theorem for operators (Chen and Chen, 1995; Lu et al., 2021). In particular, we construct a parametric map by a neural network  $\Gamma : \mathcal{A} \times \Theta \rightarrow \mathcal{U}$  for a finite-dimensional parameter space  $\Theta$  to approximate the true solution operator  $\Gamma^\dagger$ . In this paper, we adopt the *DeepONet* architecture (Lu et al., 2021), suitable for their ability to learn mappings from pairings of initial input data (Tan and Chen, 2022), to model  $\Gamma$ . We refer the readers to Appendix F for some basics of DeepONet and its enhanced versions. Then, the neural operator learning problem for finding the optimal  $\theta^* \in \Theta$  can be done in the classical risk minimization framework via

$$\begin{aligned} \theta^* = \operatorname{argmin}_{\theta \in \Theta} \quad & \mathbb{E}_{(a, u_0, u_T) \sim \mu} \left[ \left\| (\partial_t + \mathcal{D})\Gamma(a, \theta) \right\|_{L^2(\Omega \times (0, T))}^2 \right. \\ & \left. + \lambda_0 \left\| \Gamma(a, \theta)(\cdot, 0) - u_0 \right\|_{L^2(\Omega)}^2 + \lambda_T \left\| \Gamma(a, \theta)(\cdot, T) - u_T \right\|_{L^2(\Omega)}^2 \right], \end{aligned} \quad (9)$$

where the input data  $(a, u_0, u_T)$  are sampled from some joint distribution  $\mu$ . In (9), we minimize the PDE residual corresponding to  $\partial_t u + \mathcal{D}[u] = 0$  while constraining the network by imposing boundary conditions. The loss function has weights  $\lambda_0, \lambda_T > 0$ . Given a finite sample  $\{(a^{(i)}, u_0^{(i)}, u_T^{(i)})\}_{i=1}^n$ , and data points randomly sampled in the space-time domain  $\Omega \times (0, T)$ , we may minimize the empirical loss analog of (9) by replacing  $\|\cdot\|_{L^2(\Omega \times (0, T))}$  with the discrete  $L^2$  norm over domain  $\Omega \times (0, T)$ . Computation of the exact differential operators  $\partial_t$  and  $\mathcal{D}$  can be conveniently exploited via automatic differentiation in standard deep learning packages.

Neural operators offer advantages over more traditional neural networks that typically depend on some fixed mesh discretization into a finite-dimensional space and require the retraining for each different input  $(a, u_0, u_T)$  to the dynamical system (8). In contrast, neural operators performs amortized inference to learn the dynamics for a family of inputs and thus no retraining is needed for the subsequent inference stage. In addition, neural operators are flexible enough to transmute context from the original problem into a more targeted task, producing a discretization-invariant approach that often achieves more desirable results such as in the zero-shot super-resolution applications. See more details in Section 4.3.

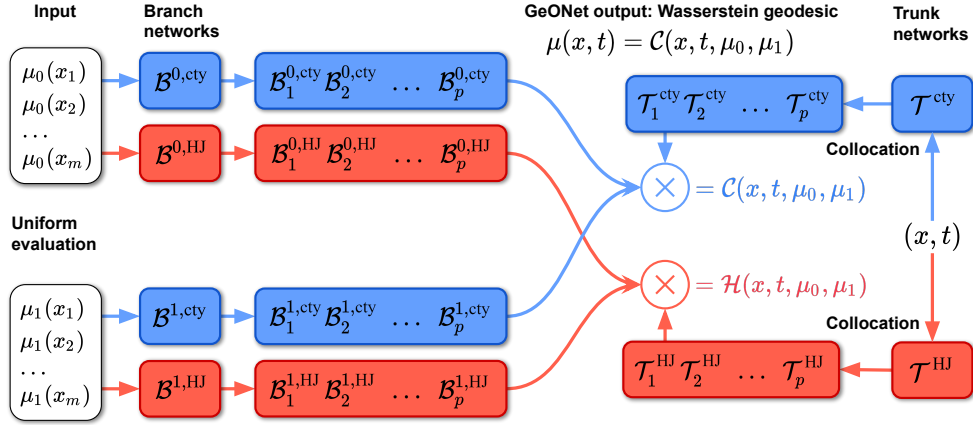


Figure 2: Architecture of GeONet, containing six neural networks to solve the continuity and Hamilton-Jacobi (HJ) equations, three for each. We minimize the total loss, and the continuity solution yields the geodesic. GeONet branches and trunks output vectors of dimension  $p$ , in which we perform multiplication among neural network elements to produce the continuity and HJ solutions.

### 3 OUR METHOD

We present *GeONet*, a geodesic operator network for learning the Wasserstein geodesic  $\{\mu_t\}_{t \in [0,1]}$  connecting  $\mu_0$  to  $\mu_1$  from the distance  $W_2(\mu_0, \mu_1)$ . Let  $\Omega \subset \mathbb{R}^d$  be the spatial domain where the probability measures are supported. For probability measures  $\mu_0, \mu_1 \in \mathcal{P}_2(\Omega)$ , it is well-known that the constant-speed geodesic  $\{\mu_t\}_{t \in [0,1]}$  between  $\mu_0$  and  $\mu_1$  is an absolutely continuous curve in the metric space  $(\mathcal{P}_2(\Omega), W_2)$ , which we denote as  $\text{AC}(\mathcal{P}_2(\Omega))$ .  $\mu_t$  solves the kinetic energy minimization problem in (4) (Santambrogio, 2015). Some basic facts on the metric geometry structure of the Wasserstein geodesic and its relation to the fluid dynamic formulation are reviewed and discussed in Appendix C. In this work, our goal is to learn a non-linear operator

$$\Gamma^\dagger : \mathcal{P}_2(\Omega) \times \mathcal{P}_2(\Omega) \rightarrow \text{AC}(\mathcal{P}_2(\Omega)), \quad (10)$$

$$(\mu_0, \mu_1) \mapsto \{\mu_t\}_{t \in [0,1]}, \quad (11)$$

based on a training dataset  $\{(\mu_0^{(1)}, \mu_1^{(1)}), \dots, (\mu_0^{(n)}, \mu_1^{(n)})\}$ . The core idea of GeONet is to learn the KKT optimality condition (7) for the Benamou-Brenier problem. Since (7) is derived to ensure the zero duality gap between the primal and dual dynamic OT problems, solving the Wasserstein geodesic requires us to introduce two sets of neural networks that train the coupled PDEs simultaneously. Specifically, we model the operator learning problem as an enhanced version of the unstacked DeepONet architecture (Lu et al., 2021; Tan and Chen, 2022) by jointly training three primal networks in (12) and three dual networks in (13) as follows:

$$\mathcal{C}(\mu_0, \mu_1)(x, t, \phi) = \sum_{k=1}^p \mathcal{B}_k^{0,\text{cty}}(\mu_0, \theta^{0,\text{cty}}) \cdot \mathcal{B}_k^{1,\text{cty}}(\mu_1, \theta^{1,\text{cty}}) \cdot \mathcal{T}_k^{\text{cty}}(x, t, \xi^{\text{cty}}), \quad (12)$$

$$\mathcal{H}(\mu_0, \mu_1)(x, t, \psi) = \sum_{k=1}^p \mathcal{B}_k^{0,\text{HJ}}(\mu_0, \theta^{0,\text{HJ}}) \cdot \mathcal{B}_k^{1,\text{HJ}}(\mu_1, \theta^{1,\text{HJ}}) \cdot \mathcal{T}_k^{\text{HJ}}(x, t, \xi^{\text{HJ}}), \quad (13)$$

where  $\mathcal{B}^{j,\text{cty}}(\mu_j(x_1), \dots, \mu_j(x_m), \theta^{j,\text{cty}}) : \mathbb{R}^m \times \Theta \rightarrow \mathbb{R}^p$  and  $\mathcal{B}^{j,\text{HJ}}(\mu_j(x_1), \dots, \mu_j(x_m), \theta^{j,\text{HJ}}) : \mathbb{R}^m \times \Theta \rightarrow \mathbb{R}^p$  are *branch* neural networks taking  $m$ -discretized input of initial and terminal density values at  $j = 0$  and  $j = 1$  respectively, and  $\mathcal{T}^{\text{cty}}(x, t, \xi^{\text{cty}}) : \mathbb{R}^d \times [0, 1] \times \Xi \rightarrow \mathbb{R}^p$  and  $\mathcal{T}^{\text{HJ}}(x, t, \xi^{\text{HJ}}) : \mathbb{R}^d \times [0, 1] \times \Xi \rightarrow \mathbb{R}^p$  are *trunk* neural networks taking spatial and temporal inputs (cf. Appendix F for more details on DeepONet models). Here  $\Theta$  and  $\Xi$  are finite-dimensional parameter spaces, and  $p$  is the output dimension of the branch and truck networks. Denote parameter concatenations  $\phi := (\theta^{0,\text{cty}}, \theta^{1,\text{cty}}, \xi^{\text{cty}})$  and  $\psi := (\theta^{0,\text{HJ}}, \theta^{1,\text{HJ}}, \xi^{\text{HJ}})$ . Then the primal operator network  $\mathcal{C}_\phi(x, t, \mu_0, \mu_1) := \mathcal{C}(x, t, \mu_0, \mu_1, \phi)$  for  $\phi \in \Theta \times \Theta \times \Xi$  acts as an approximate solution to the continuity equation, hence the true geodesic  $\Gamma^\dagger(x, t, \mu_0(x), \mu_1(x)) := \mu_t(x) = \mu(x, t)$ , while

the dual operator network  $\mathcal{H}_\psi(x, t, \mu_0, \mu_1)$  for  $\psi \in \Theta \times \Theta \times \Xi$  corresponds to that of the associated Hamilton-Jacobi equation. The architecture of GeONet is shown in Figure 2.

To train the GeONet defined in (12) and (13), we minimize the empirical loss function corresponding to the system of primal-dual PDEs and boundary residuals in (7) over the parameter space  $\Theta \times \Theta \times \Xi$ :

$$\phi^*, \psi^* = \operatorname{argmin}_{\phi, \psi \in \Theta \times \Theta \times \Xi} \mathcal{L}_{\text{cty}} + \mathcal{L}_{\text{HJ}} + \mathcal{L}_{\text{BC}}, \quad (14)$$

where  $\mathcal{L}_{\text{cty}} = \sum_{i=1}^n \mathcal{L}_{\text{cty},i}$ ,  $\mathcal{L}_{\text{HJ}} = \sum_{i=1}^n \mathcal{L}_{\text{HJ},i}$ ,  $\mathcal{L}_{\text{BC}} = \sum_{i=1}^n \mathcal{L}_{\text{BC},i}$ , and

$$\mathcal{L}_{\text{cty},i} = \frac{\alpha_1}{N} \left\| \frac{\partial}{\partial t} \mathcal{C}_{\phi,i}(x, t) + \operatorname{div}(\mathcal{C}_{\phi,i}(x, t) \nabla \mathcal{H}_{\psi,i}(x, t)) \right\|_{L^2(\Omega \times (0,1))}^2, \quad (15)$$

$$\mathcal{L}_{\text{HJ},i} = \frac{\alpha_2}{N} \left\| \frac{\partial}{\partial t} \mathcal{H}_{\psi,i}(x, t) + \frac{1}{2} \|\nabla \mathcal{H}_{\psi,i}(x, t)\|_2^2 \right\|_{L^2(\Omega \times (0,1))}^2, \quad (16)$$

$$\mathcal{L}_{\text{BC},i} = \frac{\beta_0}{N} \left\| \mathcal{C}_{\phi,i}(x, 0) - \mu_0^{(i)} \right\|_{L^2(\Omega)}^2 + \frac{\beta_1}{N} \left\| \mathcal{C}_{\phi,i}(x, 1) - \mu_1^{(i)} \right\|_{L^2(\Omega)}^2. \quad (17)$$

Here,  $\mathcal{C}_{\phi,i}(x, t) := \mathcal{C}_\phi(x, t, \mu_0^{(i)}(x), \mu_1^{(i)}(x))$  and  $\mathcal{C}_{\phi,t,i}(x) := \mathcal{C}_\phi(x, t, \mu_0^{(i)}(x), \mu_1^{(i)}(x))$  denote the evaluation of neural network  $\mathcal{C}_\phi$  over the  $i$ -th distribution of the  $n$  training data at space location  $x$  and time point  $t$ . The same notation applies for the Hamilton-Jacobi neural networks.  $\mathcal{L}_{\text{cty}}$  is the loss component in which the continuity equation is satisfied, and  $\mathcal{L}_{\text{HJ}}$  is the Hamilton-Jacobi equation loss component. The boundary conditions are incorporated in the  $\mathcal{L}_{\text{BC}}$  term, and  $\alpha_1, \alpha_2, \beta_0, \beta_1$  are weights for the strength to impose the physics-informed loss. Automatic differentiation of our GeONet involves differentiating the coupled DeepONet architecture (cf. Figure 2) in order to compute the physics-informed loss terms.

One iterate of our training procedure is as follows. We first select a collection of  $N$  indices  $\mathcal{I}$  from 1 to  $n$  for which of the  $n$  distributions are to be evaluated, with possible repeats. For the physics terms, following (Raissi et al., 2019), we utilize a *collocation* procedure as follows. We sample  $N$  pairs  $(x, t)$  randomly and uniformly within the bounded domain  $\Omega \times [0, 1]$ . These pairs are resampled during each training iteration in our method. Then, we evaluate the continuity and Hamilton-Jacobi residuals displayed in (15) and (16) at such sampled values, in which the loss is subsequently minimized with the corresponding indices in  $\mathcal{I}$ , making the norms approximated as discrete. For branch input, we take equispaced locations  $x_1, \dots, x_m$  within  $\Omega$ , a bounded domain in  $\mathbb{R}^d$ , typically a hypercube  $\tilde{\Omega}$ . Then the  $N$  branch locations are evaluated among  $\tilde{\Omega}$  as well for the BC loss.

It is worth highlighting that GeONet is mesh invariant in the sense that geodesics can be evaluated along any location of space and time and no output mesh is needed. The uniform collocation procedure ensures all areas in space and time of the geodesic are considered in training. In contrast, DeepONets do indeed take sample points along some predetermined grid; however, the geodesic itself is perfectly mesh invariant and can be evaluated at any point in space and time. Only the neural network input for the branches scales in length as the initial condition input length scales.

**Modified multi-layer perceptron (MLP).** A modified MLP architecture as described in (Wang et al., 2021) has been shown to have great ability in improving performance for PINNs and physics-informed DeepONets. We elaborate on this architecture in Appendix G and describe our empirical findings with this modified MLP for GeONet in Appendix I.

**Entropic regularization.** Our GeONet is compatible with entropic regularization, which is related to the Schrödinger bridge problem and stochastic control (Chen et al., 2016). In Appendix D, we propose the *entropic-regularized GeONet* (ER-GeONet), which learns a similar system of KKT conditions for the optimization as in (7). In the zero-noise limit as the entropic regularization parameter  $\varepsilon \downarrow 0$ , the solution of the optimal entropic interpolating flow converges to solution of the Benamou-Brenier problem (4) in the sense of the method of vanishing viscosity (Mikami, 2004; Evans, 2010).

## 4 NUMERICAL EXPERIMENTS

### 4.1 GAUSSIAN MIXTURE DISTRIBUTIONS

Since finite mixture distributions are powerful universal approximators for continuous probability density functions (Nguyen et al., 2020), we first deploy GeONet on Gaussian mixture distributions

over domains of varying dimensions. We learn the Wasserstein geodesic mapping between two distributions of the form  $\mu_j(x) = \sum_{i=1}^{k_j} \pi_i \mathcal{N}(x|u_i, \Sigma_i)$  subject to  $\sum_{i=1}^{k_j} \pi_i = 1$ , where  $j \in \{0, 1\}$  corresponds to initial and terminal distributions  $\mu_0, \mu_1$ , and  $k_j$  denotes the number of components in the mixture. Here  $u_i$  and  $\Sigma_i$  are the mean vectors and covariance matrices of individual Gaussian components respectively. Due to the space limit, we defer simulation setups and model training details to Appendices H and I.

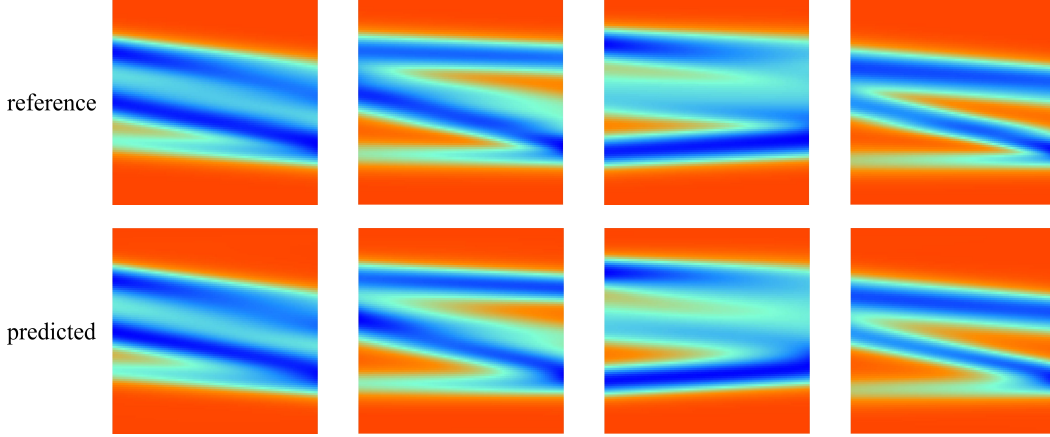


Figure 3: Four unique geodesics predicted by GeONet with reference geodesics computed by POT on test univariate Gaussian mixture distribution pairs with  $k_0 = k_1 = 6$ . The reference serves as a close approximation to the true geodesic due to entropic regularization. The vertical axis is space and the horizontal axis is time.

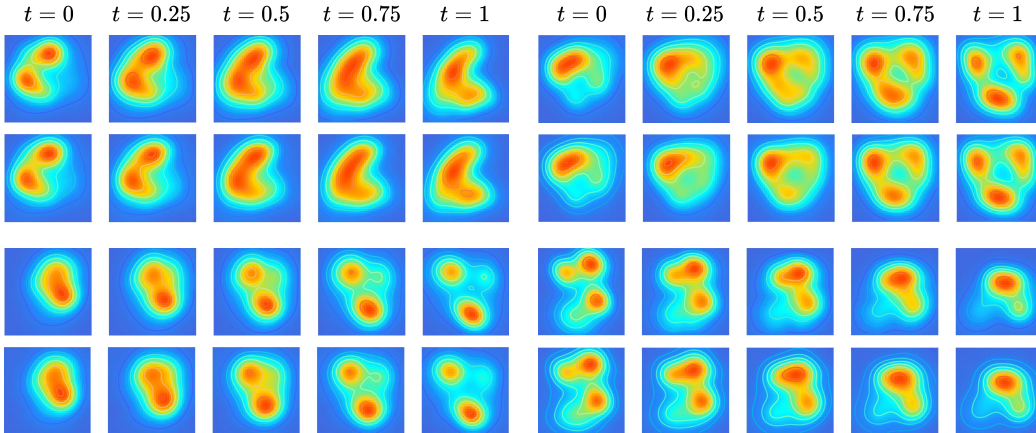


Figure 4: Geodesics predicted by GeONet on bivariate Gaussians over a square domain. The top of each pair is the reference solution computed by POT, and the bottom is GeONet.

**Error metric.** We use the  $L^1$  error  $\int_{\Omega} |\mathcal{C} - \mu| dx$  as our error metric to assess the performance, where  $\mu := \mu(x, t)$  is a reference geodesic as proxy of the true geodesic without entropic regularization. The  $L^1$  error integral is estimated by evaluating a discrete Riemann sum along a mesh and the reference is computed using the Convolutional Wasserstein Barycenter framework within the POT Python library (Solomon et al., 2015; Flamary et al., 2021). Since  $\int_{\Omega} |\mu| dx = 1$  for all time points, the  $L^1$  error is also a relative error, a meaningful metric essentially corresponding to the percentage error between the neural operator geodesic and the reference. We examine errors in regard to an identity geodesic (i.e.,  $\mu_0 = \mu_1$ ), a random test pairing, and an out-of-distribution (OOD) pairing.



Table 2: Relative  $L^1$  error of GeONet on 50 test data of univariate and bivariate Gaussian mixtures. We report the means and standard deviations as a percentage, making all values multiplied by  $10^{-2}$ .

Experiment	GeONet error for Gaussian mixtures				
	$t = 0$	$t = 0.25$	$t = 0.5$	$t = 0.75$	$t = 1$
1D identity	$2.67 \pm 0.750$	$2.85 \pm 0.912$	$3.04 \pm 1.02$	$2.86 \pm 0.898$	$2.63 \pm 0.696$
1D random	$4.92 \pm 2.00$	$5.43 \pm 3.02$	$5.76 \pm 3.56$	$5.26 \pm 3.25$	$4.65 \pm 1.50$
1D OOD	$12.9 \pm 4.13$	$14.3 \pm 5.35$	$16.4 \pm 6.01$	$14.9 \pm 5.48$	$12.3 \pm 3.94$
2D identity	$6.50 \pm 1.15$	$7.68 \pm 0.915$	$7.69 \pm 0.924$	$7.70 \pm 0.889$	$6.42 \pm 1.11$
2D random	$6.59 \pm 1.01$	$7.10 \pm 0.869$	$7.13 \pm 0.892$	$7.04 \pm 0.780$	$6.33 \pm 0.835$
2D OOD	$7.15 \pm 0.985$	$7.82 \pm 1.04$	$8.14 \pm 1.33$	$7.96 \pm 1.30$	$7.14 \pm 0.882$

#### 4.2 A REAL DATA APPLICATION

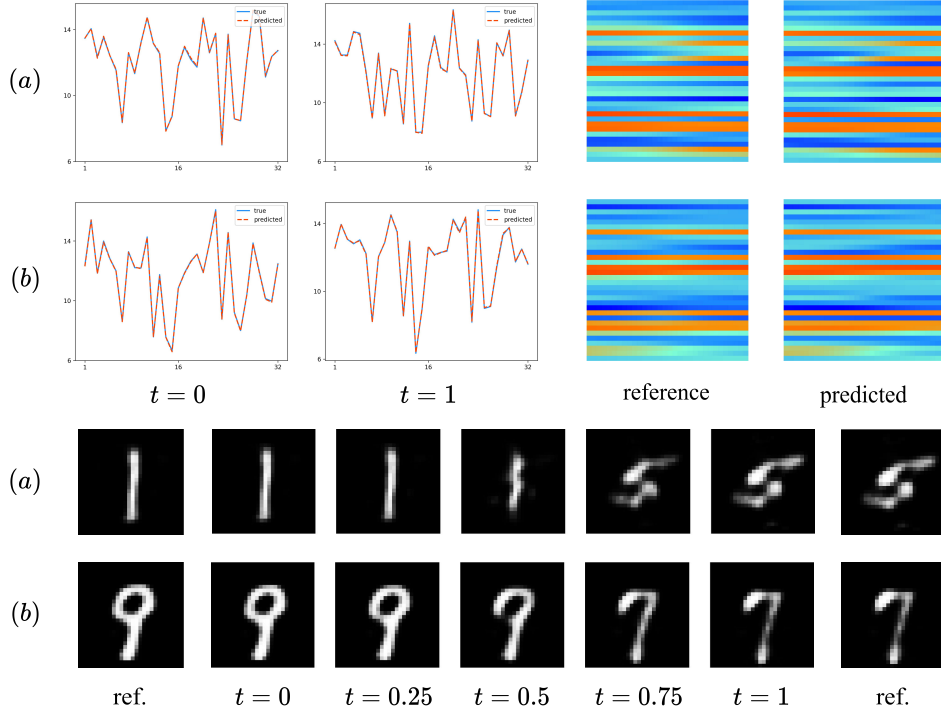


Figure 5: Beginning from top left and going clockwise, we display the initial conditions in the encoded space, the geodesics in the encoded space, and the decoded geodesics as  $28 \times 28$  images. (a) and (b) correspond to two unique pairings.

Our next experiment was upon the MNIST dataset of  $28 \times 28$  images of single-digit numbers. It is difficult for GeONet to capture the geodesics between digits: unlike Gaussian mixtures, MNIST resembles jump-discontinuous data, and relatively piecewise constant otherwise, which is troublesome for the physics-informed term. To remedy our problems with MNIST, we use a pretrained autoencoder to encode the MNIST digits into a low-dimensional representation  $v \in \mathbb{R}^{32}$  with an encoder  $\Phi$  and a decoder  $\Phi^{-1} : v \rightarrow \mathbb{R}^{28} \times \mathbb{R}^{28}$  mapping the encoded representation into newly-formed digits resembling that which was fed into the encoder. We institute GeONet upon the encoded representations, learning the geodesic between highly irregular encoded data. Figure 5 shows the learnt geodesics in the encoded space and decoded images on the geodesics.

#### 4.3 ZERO-SHOT SUPER-RESOLUTION APPLICATION



Table 3: Relative  $L^1$  error of GeONet on 50 test pairings of encoded MNIST. The error must be normalized to be relative in this experiment. All values are multiplied by  $10^{-2}$  if not viewed as a percentage. Error was calculated upon the geodesic of the shifted data in the encoded space. We use  $p = 200$ .

Testing setting	GeONet error on encoded MNIST data				
	$t = 0$	$t = 0.25$	$t = 0.5$	$t = 0.75$	$t = 1$
Identity	$1.68 \pm 0.401$	$2.79 \pm 0.640$	$3.13 \pm 0.696$	$2.82 \pm 0.638$	$1.93 \pm 0.621$
Random	$1.94 \pm 0.594$	$4.08 \pm 1.02$	$5.96 \pm 1.66$	$4.01 \pm 1.03$	$2.09 \pm 0.522$

The mesh-invariant nature of the output of GeONet allows it is suitable for zero-shot super-resolution examples of adapting low-resolution data into high-resolution geodesics, which includes initial data at  $t = 0, 1$ . The neural operator can be trained only on such low-resolution information, and the super-resolution application results from the uniform sampling done within the training and physics-informed loss. On the contrary, traditional OT solvers have no ability to do this, as they are confined to the original mesh. In Figure 6, a  $24 \times 24$  initial condition which is used as neural operator input is adapted to an  $80 \times 80$  image, which can be done for all intermediate and boundary times on the geodesic.

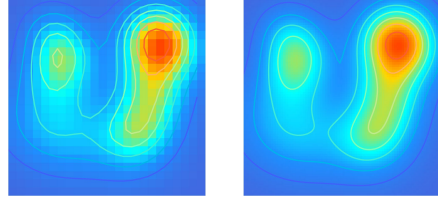


Figure 6: A zero-shot super-resolution of a bivariate Gaussian mixture initial condition example. A lower- to higher-resolution geodesic is produced.

#### 4.4 RUNTIME COMPARISON

Inference of GeONet is instantaneous, a feature advantageous for many pairs and high resolution images, especially if geodesics are needed quickly. POT is greatly encumbered by a fine mesh. Figure 7 (right) demonstrates an inference-stage runtime comparison of GeONet to the POT algorithms on Gaussian mixtures considered in Section 4.1. The POT algorithm was minimally modified, only so that the pertinent distributions could be taken as input. The linear pattern of Figure 7 (right) on log-scale suggests the computational improvement of GeONet over POT is of the orders of magnitude. In Figure 7, the number of time discretization is 20 for univariate, and 5 for bivariate. The time to create the data is not considered in the figure. More training details can be found in Appendix H.

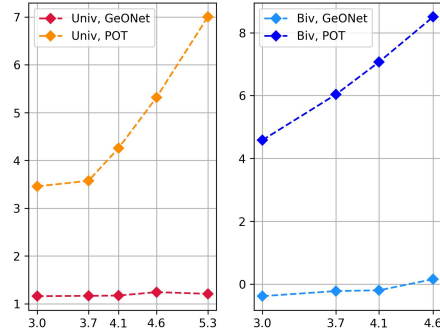


Figure 7: Comparison of log-runtime in seconds on Gaussian mixtures. The y-axis is the log of time, the x-axis is the log of grid length in one dimension. We total over 50 density pairs.

#### 4.5 LIMITATIONS

GeONet’s branch network input exponentially increases in spatial dimension, necessitating extensive input data even in moderately high-dimensional scenarios. One strategy to mitigate this is through leveraging low-dimensional data representations as in the MNIST experiment. While traditional geodesic solvers primarily handle one or two dimensions, GeONet offers a versatile alternative, accommodating any dimension at the cost of potential computational precision. Moreover, GeONet mandates predetermined evaluation points for branch input, a requisite grounded in the pairing of initial conditions. It is of interest to extend GeONet to include training input data pair on different resolutions.

---

## REFERENCES

- Jason Altschuler, Jonathan Weed, and Philippe Rigollet. Near-linear time approximation algorithms for optimal transport via sinkhorn iteration. In *Proceedings of the 31st International Conference on Neural Information Processing Systems*, NIPS’17, page 1961–1971, Red Hook, NY, USA, 2017. Curran Associates Inc. ISBN 9781510860964.
- Luigi Ambrosio, Nicola Gigli, and Giuseppe Savaré. *Gradient Flows in Metric Spaces and in the Space of Probability Measures*. Lectures in Mathematics ETH Zürich. Birkhäuser Baseluser Basel, second edition, 2008.
- Martin Arjovsky, Soumith Chintala, and Léon Bottou. Wasserstein generative adversarial networks. In Doina Precup and Yee Whye Teh, editors, *Proceedings of the 34th International Conference on Machine Learning*, volume 70 of *Proceedings of Machine Learning Research*, pages 214–223. PMLR, 06–11 Aug 2017. URL <https://proceedings.mlr.press/v70/arjovsky17a.html>.
- Jean-David Benamou and Yann Brenier. A computational fluid mechanics solution to the monge-kantorovich mass transfer problem. *Numerische Mathematik*, 84:375–393, 2000.
- Jean-David Benamou, Guillaume Carlier, Marco Cuturi, Luca Nenna, and Gabriel Peyré. Iterative bregman projections for regularized transportation problems. *SIAM Journal on Scientific Computing*, 37(2):A1111–A1138, 2015. doi: 10.1137/141000439. URL <https://doi.org/10.1137/141000439>.
- Dimitri P. Bertsekas and David A. Castanon. The auction algorithm for the transportation problem. *Annals of Operations Research*, 20(1):67–96, December 1989. ISSN 0254-5330. doi: 10.1007/BF02216923.
- Yann Brenier. Polar factorization and monotone rearrangement of vector-valued functions. *Communications on Pure and Applied Mathematics*, 44(4):375–417, 1991. doi: <https://doi.org/10.1002/cpa.3160440402>. URL <https://onlinelibrary.wiley.com/doi/abs/10.1002/cpa.3160440402>.
- Dmitri Burage, Yuri Burago, and Sergei Ivanov. *A Course in Metric Geometry*. Graduate studies in mathematics. American mathematical society, Providence, Rhode Island, 2001.
- Tianping Chen and Hong Chen. Universal approximation to nonlinear operators by neural networks with arbitrary activation functions and its application to dynamical systems. *IEEE Transactions on Neural Networks*, 6(4):911–917, 1995. doi: 10.1109/72.392253.
- Xiaohui Chen and Yun Yang. Cutoff for exact recovery of gaussian mixture models. *IEEE Transactions on Information Theory*, 67(6):4223–4238, 2021. doi: 10.1109/TIT.2021.3063155.
- Yongxin Chen, Tryphon T. Georgiou, and Michele Pavon. On the relation between optimal transport and schrödinger bridges: A stochastic control viewpoint. *Journal of Optimization Theory and Applications*, 169(2):671–691, 2016. doi: 10.1007/s10957-015-0803-z. URL <https://doi.org/10.1007/s10957-015-0803-z>.
- Yongxin Chen, Tryphon T. Georgiou, and Michele Pavon. Optimal transport in systems and control. *Annual Review of Control, Robotics, and Autonomous Systems*, 4(1):89–113, 2021. doi: 10.1146/annurev-control-070220-100858. URL <https://doi.org/10.1146/annurev-control-070220-100858>.
- Nicolas Courty, Rémi Flamary, Devis Tuia, and Alain Rakotomamonjy. Optimal transport for domain adaptation. *IEEE Transactions on Pattern Analysis and Machine Intelligence*, 39(9):1853–1865, 2017. doi: 10.1109/TPAMI.2016.2615921.
- Marco Cuturi. Sinkhorn distances: Lightspeed computation of optimal transport. In C.J. Burges, L. Bottou, M. Welling, Z. Ghahramani, and K.Q. Weinberger, editors, *Advances in Neural Information Processing Systems*, volume 26. Curran Associates, Inc., 2013. URL <https://proceedings.neurips.cc/paper/2013/file/af21d0c97db2e27e13572cbf59eb343d-Paper.pdf>.

- 
- Pavel Dvurechensky, Alexander Gasnikov, and Alexey Kroshnin. Computational optimal transport: Complexity by accelerated gradient descent is better than by sinkhorn’s algorithm. In Jennifer Dy and Andreas Krause, editors, *Proceedings of the 35th International Conference on Machine Learning*, volume 80 of *Proceedings of Machine Learning Research*, pages 1367–1376. PMLR, 10–15 Jul 2018.
- Lawrence C. Evans. *Partial Differential Equations*. American Mathematical Society, Providence, R.I., 2010. ISBN 9780821849743 0821849743.
- Chris Finlay, Jörn-Henrik Jacobsen, Levon Nurbekyan, and Adam M Oberman. "how to train your neural ode: the world of jacobian and kinetic regularization". In *ICML*, 2020.
- Rémi Flamary, Nicolas Courty, Alexandre Gramfort, Mokhtar Z. Alaya, Aurélie Boissunon, Stanislas Chambon, Laetitia Chapel, Adrien Corenflos, Kilian Fatras, Nemo Fournier, Léo Gautheron, Nathalie T.H. Gayraud, Hicham Janati, Alain Rakotomamonjy, Ievgen Redko, Antoine Rolet, Antony Schutz, Vivien Seguy, Danica J. Sutherland, Romain Tavenard, Alexander Tong, and Titouan Vayer. Pot: Python optimal transport. *Journal of Machine Learning Research*, 22(78):1–8, 2021.
- Aude Genevay, Marco Cuturi, Gabriel Peyré, and Francis Bach. Stochastic optimization for large-scale optimal transport. In *Proceedings of the 30th International Conference on Neural Information Processing Systems, NIPS’16*, page 3440–3448, Red Hook, NY, USA, 2016. Curran Associates Inc. ISBN 9781510838819.
- Samuel J. Gershman and Noah D. Goodman. Amortized inference in probabilistic reasoning. *Cognitive Science*, 36, 2014.
- Daisuke Inoue, Yuji Ito, and Hiroaki Yoshida. Optimal transport-based coverage control for swarm robot systems: Generalization of the voronoi tessellation-based method. In *2021 American Control Conference (ACC)*, pages 3032–3037, 2021. doi: 10.23919/ACC50511.2021.9483194.
- Marcel Klatt, Carla Tameling, and Axel Munk. Empirical regularized optimal transport: Statistical theory and applications. *SIAM Journal on Mathematics of Data Science*, 2(2):419–443, 2020. doi: 10.1137/19M1278788.
- Nikola Kovachki, Zongyi Li, Burigede Liu, Kamyar Azizzadenesheli, Kaushik Bhattacharya, Andrew Stuart, and Anima Anandkumar. Neural operator: Learning maps between function spaces, 2021. URL <https://arxiv.org/abs/2108.08481>.
- Vishaal Krishnan and Sonia Martínez. Distributed optimal transport for the deployment of swarms. In *2018 IEEE Conference on Decision and Control (CDC)*, pages 4583–4588, 2018. doi: 10.1109/CDC.2018.8619816.
- H. W. Kuhn. The hungarian method for the assignment problem. *Naval Research Logistics Quarterly*, 2(1-2):83–97, 1955. doi: <https://doi.org/10.1002/nav.3800020109>. URL <https://onlinelibrary.wiley.com/doi/abs/10.1002/nav.3800020109>.
- Matt J. Kusner, Yu Sun, Nicholas I. Kolkin, and Kilian Q. Weinberger. From word embeddings to document distances. In *Proceedings of the 32nd International Conference on International Conference on Machine Learning - Volume 37, ICML’15*, page 957–966. JMLR.org, 2015.
- Zongyi Li, Nikola Kovachki, Kamyar Azizzadenesheli, Burigede Liu, Kaushik Bhattacharya, Andrew Stuart, and Anima Anandkumar. Neural operator: Graph kernel network for partial differential equations, 2020a. URL <https://arxiv.org/abs/2003.03485>.
- Zongyi Li, Nikola Kovachki, Kamyar Azizzadenesheli, Burigede Liu, Kaushik Bhattacharya, Andrew Stuart, and Anima Anandkumar. Fourier neural operator for parametric partial differential equations, 2020b. URL <https://arxiv.org/abs/2010.08895>.
- Zongyi Li, Hongkai Zheng, Nikola Kovachki, David Jin, Haoxuan Chen, Burigede Liu, Kamyar Azizzadenesheli, and Anima Anandkumar. Physics-informed neural operator for learning partial differential equations, 2021. URL <https://arxiv.org/abs/2111.03794>.

- 
- Shu Liu, Shaojun Ma, Yongxin Chen, Hongyuan Zha, and Haomin Zhou. Learning high dimensional wasserstein geodesics, 2021. URL <https://arxiv.org/abs/2102.02992>.
- Lu Lu, Pengzhan Jin, Guofei Pang, Zhongqiang Zhang, and George Em Karniadakis. Learning nonlinear operators via deeponet based on the universal approximation theorem of operators. *Nat Mach Intell*, 3:218–229, 2021.
- David G. Luenberger and Yinyu Ye. *Linear and Nonlinear Programming*. Springer Publishing Company, Incorporated, 2015. ISBN 3319188410.
- Robert J. McCann. A convexity principle for interacting gases. *Advances in Mathematics*, 128(1): 153–179, 1997. URL <https://www.sciencedirect.com/science/article/pii/S0001870897916340>.
- Toshio Mikami. Monge’s problem with a quadratic cost by the zero-noise limit of h-path processes. *Probability Theory and Related Fields*, 129(2):245–260, 2004. doi: 10.1007/s00440-004-0340-4. URL <https://doi.org/10.1007/s00440-004-0340-4>.
- T. Tin Nguyen, Hien D. Nguyen, Faicel Chamroukhi, and Geoffrey J. McLachlan. Approximation by finite mixtures of continuous density functions that vanish at infinity. *Cogent Mathematics & Statistics*, 7(1):1750861, 2020. doi: 10.1080/25742558.2020.1750861. URL <https://doi.org/10.1080/25742558.2020.1750861>.
- Gabriel Peyré and Marco Cuturi. Computational optimal transport. *Foundations and Trends in Machine Learning*, 11(5-6):355–607, 2019.
- M. Raissi, P. Perdikaris, and G.E. Karniadakis. Physics-informed neural networks: A deep learning framework for solving forward and inverse problems involving nonlinear partial differential equations. *Journal of Computational Physics*, 378:686–707, 2019. ISSN 0021-9991. doi: <https://doi.org/10.1016/j.jcp.2018.10.045>. URL <https://www.sciencedirect.com/science/article/pii/S0021999118307125>.
- Filippo Santambrogio. *Optimal Transport for Applied Mathematicians. Calculus of Variations, PDEs and Modeling*. Birkhäuser Basel, 1 edition, 2015. URL <https://www.math.u-psud.fr/~filippo/OTAM-cvgmt.pdf>.
- Assaf Shocher, Nadav Cohen Cohen, and Michal Irani. “zero-shot” super-resolution using deep internal learning. In *The IEEE Conference on Computer Vision and Pattern Recognition (CVPR)*, June 2018.
- Richard Sinkhorn. A Relationship Between Arbitrary Positive Matrices and Doubly Stochastic Matrices. *The Annals of Mathematical Statistics*, 35(2):876 – 879, 1964. doi: 10.1214/aoms/1177703591. URL <https://doi.org/10.1214/aoms/1177703591>.
- Justin Solomon, Fernando de Goes, Gabriel Peyré, Marco Cuturi, Adrian Butscher, Andy Nguyen, Tao Du, and Leonidas Guibas. Convolutional wasserstein distances: Efficient optimal transportation on geometric domains. *ACM Trans. Graph.*, 34(4), jul 2015. ISSN 0730-0301. doi: 10.1145/2766963. URL <https://doi.org/10.1145/2766963>.
- Lesley Tan and Liang Chen. Enhanced deeponet for modeling partial differential operators considering multiple input functions, 2022. URL <https://arxiv.org/abs/2202.08942>.
- Cédric Villani. *Topics in optimal transportation*. Graduate studies in mathematics. American mathematical society, Providence, Rhode Island, 2003. ISBN 0-8218-3312-X.
- Sifan Wang, Hanwen Wang, and Paris Perdikaris. Learning the solution operator of parametric partial differential equations with physics-informed deeponets. *CoRR*, abs/2103.10974, 2021. URL <https://arxiv.org/abs/2103.10974>.
- Jeremy Yu, Lu Lu, Xuhui Meng, and George Em Karniadakis. Gradient-enhanced physics-informed neural networks for forward and inverse pde problems. *Computer Methods in Applied Mechanics and Engineering*, 393:114823, 2022. ISSN 0045-7825. doi: <https://doi.org/10.1016/j.cma.2022.114823>. URL <https://www.sciencedirect.com/science/article/pii/S0045782522001438>.

## A TRAINING ALGORITHM

---

### Algorithm 1 End-to-end training of GeONet

---

**Input:** data pairs  $(\mu_0^{(1)}, \mu_1^{(1)}), \dots, (\mu_0^{(n)}, \mu_1^{(n)})$ ; batch size  $N$ ; initialization of the neural network parameters  $\phi, \psi \in \Theta \times \Theta \times \Xi$ ; weight parameters  $\alpha_1, \alpha_2, \beta_0, \beta_1$ ; domain  $\Omega$  and branch domain (mesh)  $\tilde{\Omega}$ ; denote  $i \in \{1, \dots, N\}$ .

- 1: **while**  $\mathcal{L}_{\text{total}}$  has not converged **do**
- 2:   Independently draw  $N$  sample points from  $U(\Omega) \times U(0, 1)$ ,  $N$  points from  $U(\tilde{\Omega})$ , and  $N$  density pairs from  $\{(\mu_0^{(\ell)}, \mu_1^{(\ell)})\}_{\ell=1}^n$ , possibly repeating.
- 3:   Compute  $\Phi_i = \partial_t \mathcal{C}_{\phi, i} + \text{div}(\mathcal{C}_{\phi, i} \nabla \mathcal{H}_{\psi, i})$ . ▷ continuity residual
- 4:   Compute  $\Psi_i = \partial_t \mathcal{H}_{\psi, i} + \frac{1}{2} \|\nabla \mathcal{H}_{\psi, i}\|_2^2$ . ▷ Hamilton-Jacobi residual
- 5:   Compute  $B_{0, i} = \mathcal{C}_{\phi, 0, i} - \mu_0^{(i)}(x_{\tilde{\Omega}}^i)$ ,  $B_{1, i} = \mathcal{C}_{\phi, 1, i} - \mu_1^{(i)}(x_{\tilde{\Omega}}^i)$ . ▷ boundary residual
- 6:   Compute

$$\mathcal{L}_{\text{cty}} = \frac{\alpha_1}{N} \sum_{i=1}^N \Phi_i^2, \quad \mathcal{L}_{\text{HJ}} = \frac{\alpha_2}{N} \sum_{i=1}^N \Psi_i^2,$$

$$\mathcal{L}_{\text{BC}} = \frac{1}{N} \sum_{i=1}^N (\beta_0 B_{0, i}^2 + \beta_1 B_{1, i}^2),$$

- 7:   Compute  $\mathcal{L}_{\text{total}}(\phi, \psi) = \mathcal{L}_{\text{cty}} + \mathcal{L}_{\text{HJ}} + \mathcal{L}_{\text{BC}}$ .
  - 8:   Minimize  $\mathcal{L}_{\text{total}}(\phi, \psi)$  to update  $\phi$  and  $\psi$ . ▷ minimize the loss function
  - 9: **end while**
- 

## B DERIVATION OF PRIMAL-DUAL OPTIMALITY CONDITIONS FOR DYNAMICAL OT PROBLEM

The primal-dual analysis is a standard technique in the optimization literature such as in analyzing certain semidefinite programs (Chen and Yang, 2021). Recall the Benamou-Brenier fluid dynamics formulation of the static optimal transport problem

$$\min_{(\mu, \mathbf{v})} \int_0^1 \int_{\mathbb{R}^d} \frac{1}{2} \|\mathbf{v}(x, t)\|_2^2 \mu(x, t) \, dx \, dt \quad (18)$$

$$\text{subject to } \partial_t \mu + \text{div}(\mu \mathbf{v}) = 0, \quad (19)$$

$$\mu(\cdot, 0) = \mu_0, \quad \mu(\cdot, 1) = \mu_1. \quad (20)$$

Here, equation (19) is referred to as the *continuity equation* (CE), preserving the unit mass of the density flow  $\mu_t = \mu(\cdot, t)$ . We write the Lagrangian function for any flow  $(\mu_t)_{t \in [0, 1]}$  initializing from  $\mu_0$  and terminating at  $\mu_1$  as

$$L(\mu, \mathbf{v}, u) = \int_0^1 \int_{\mathbb{R}^d} \left[ \frac{1}{2} \|\mathbf{v}\|_2^2 \mu + (\partial_t \mu + \text{div}(\mu \mathbf{v})) u \right] \, dx \, dt, \quad (21)$$

where  $u := u(x, t)$  is the dual variable for (CE). To find the optimal solution  $\mu^*$  for the minimum kinetic energy (18), we study the saddle point optimization problem

$$\min_{(\mu, \mathbf{v}) \in (\text{CE})} \max_u L(\mu, \mathbf{v}, u), \quad (22)$$

where the minimization over  $(\mu, \mathbf{v})$  runs over all flows satisfying (CE) such that  $\mu(\cdot, 0) = \mu_0$  and  $\mu(\cdot, 1) = \mu_1$ . Note that if  $\mu \notin (\text{CE})$ , then by scaling with arbitrarily large constant, we see that

$$\max_u \int_0^1 \int_{\mathbb{R}^d} (\partial_t \mu + \text{div}(\mu \mathbf{v})) u \, dx \, dt = +\infty. \quad (23)$$

Thus,

$$\min_{(\mu, \mathbf{v}) \in (\text{CE})} \int_0^1 \int_{\mathbb{R}^d} \frac{1}{2} \|\mathbf{v}\|_2^2 \mu \, dx \, dt = \min_{(\mu, \mathbf{v})} \max_u L(\mu, \mathbf{v}, u) \quad (24)$$

$$\geq \max_u \min_{(\mu, \mathbf{v})} L(\mu, \mathbf{v}, u), \quad (25)$$

where the minimization over  $(\mu, \mathbf{v})$  is unconstrained. Using integration-by-parts and suitable decay for vanishing boundary as  $\|x\|_2 \rightarrow \infty$ , we have

$$L(\mu, \mathbf{v}, u) = \int_0^1 \int_{\mathbb{R}^d} \left[ \frac{1}{2} \|\mathbf{v}\|_2^2 \mu - \mu \partial_t u - \langle \mathbf{v}, \nabla u \rangle \mu \right] dx dt + \int_{\mathbb{R}^d} [\mu(\cdot, 1)u(\cdot, 1) - \mu(\cdot, 0)u(\cdot, 0)] dx.$$

Now, we fix  $\mu$  and  $u$ , and minimize  $L(\mu, \mathbf{v}, u)$  over  $\mathbf{v}$ . The optimal velocity vector is  $\mathbf{v}^* = \nabla u$ , and we have

$$\max_u \min_{\mu} L(\mu, \mathbf{v}^*, u) = \int_0^1 \int_{\mathbb{R}^d} \left[ - \left( \frac{1}{2} \|\nabla u\|_2^2 + \partial_t u \right) \mu \right] dx dt + \int_{\mathbb{R}^d} [u(\cdot, 1)\mu_1 - u(\cdot, 0)\mu_0] dx, \quad (26)$$

for any flow  $\mu_t$  satisfying the boundary conditions  $\mu(\cdot, 0) = \mu_0$  and  $\mu(\cdot, 1) = \mu_1$ . If  $\frac{1}{2} \|\nabla u\|_2^2 + \partial_t u \neq 0$ , then by the same scaling argument above, we have

$$\min_{\mu} \int_0^1 \int_{\mathbb{R}^d} \left[ - \left( \frac{1}{2} \|\nabla u\|_2^2 + \partial_t u \right) \mu \right] dx dt = -\infty \quad (27)$$

because  $\mu$  is unconstrained (except for the boundary conditions). Then we deduce that

$$\min_{(\mu, \mathbf{v}) \in (\text{CE})} \int_0^1 \int_{\mathbb{R}^d} \frac{1}{2} \|\mathbf{v}\|_2^2 \mu \geq \max_{u \in (\text{HJ})} \left\{ \int_{\mathbb{R}^d} u(\cdot, 1)\mu_1 - \int_{\mathbb{R}^d} u(\cdot, 0)\mu_0 \right\}, \quad (28)$$

where  $u \in (\text{HJ})$  means that  $u$  solves the *Hamilton-Jacobi equation* (HJ)

$$\partial_t u + \frac{1}{2} \|\nabla u\|_2^2 = 0. \quad (29)$$

From (28), we see that the duality gap is non-negative, and it is equal to zero if and only if  $(\mu^*, u^*)$  solves the following system of PDEs

$$\begin{cases} \partial_t \mu + \text{div}(\mu \nabla u) = 0, & \partial_t u + \frac{1}{2} \|\nabla u\|_2^2 = 0, \\ \mu(\cdot, 0) = \mu_0, & \mu(\cdot, 1) = \mu_1. \end{cases} \quad (30)$$

PDEs in (30) are referred to as the Karush–Kuhn–Tucker (KKT) conditions for the Wasserstein geodesic problem.

## C METRIC GEOMETRY STRUCTURE OF THE WASSERSTEIN SPACE AND GEODESIC

In this section, we review some basic facts on metric geometry properties of the Wasserstein space and geodesic. We first discuss the general metric space  $(X, d)$ , and then specialize to the Wasserstein (metric) space  $(\mathcal{P}_p(\mathbb{R}^d), W_p)$  for  $p \geq 1$ . Furthermore, we connect to the fluid dynamic formulation of optimal transport. Most of the materials are based on the reference books (Burage et al., 2001; Ambrosio et al., 2008; Santambrogio, 2015).

### C.1 GENERAL METRIC SPACE

*Definition C.1* (Absolutely continuous curve). Let  $(X, d)$  be a metric space. A curve  $\omega : [0, 1] \rightarrow X$  is *absolutely continuous* if there is a function  $g \in L^1([0, 1])$  such that for all  $t_0 < t_1$ , we have

$$d(\omega(t_0), \omega(t_1)) \leq \int_{t_0}^{t_1} g(\tau) d\tau. \quad (31)$$

Such curves are denoted by  $\text{AC}(X)$ .

*Definition C.2* (Metric derivative). If  $\omega : [0, 1] \rightarrow X$  is a curve in a metric space  $(X, d)$ , the *metric derivative* of  $\omega$  at time  $t$  is defined as

$$|\omega'| (t) := \lim_{h \rightarrow 0} \frac{d(\omega(t+h), \omega(t))}{|h|}, \quad (32)$$

if the limit exists.

The following theorem generalizes the classical Rademacher theorem from a Euclidean space into any metric space in terms of the metric derivative.

**Theorem C.3 (Rademacher).** If  $\omega : [0, 1] \rightarrow X$  is Lipschitz continuous, then the metric derivative  $|\omega'|(\tau)$  exists for almost every  $\tau \in [0, 1]$ . In addition, for any  $0 \leq t < s \leq 1$ , we have

$$d(\omega(t), \omega(s)) \leq \int_t^s |\omega'|(\tau) d\tau. \quad (33)$$

Theorem C.3 tells us that absolutely continuous curve  $\omega$  has a metric derivative well-defined almost everywhere, and the “length” of the curve  $\omega$  is bounded by the integral of the metric derivative. Thus, a natural definition of the length of a curve in a general metric space is to take the best approximation over all possible meshes.

**Definition C.4 (Curve length).** For a curve  $\omega : [0, 1] \rightarrow X$ , we define its *length* as

$$\text{Length}(\omega) := \sup \left\{ \sum_{k=0}^{n-1} d(\omega(t_k), \omega(t_{k+1})) : n \geq 1, 0 = t_0 < t_1 < \dots < t_n = 1 \right\}. \quad (34)$$

Note that if  $\omega \in \text{AC}(X)$ , then

$$d(\omega(t_k), \omega(t_{k+1})) \leq \int_{t_k}^{t_{k+1}} g(\tau) d\tau \quad (35)$$

so that

$$\text{Length}(\omega) \leq \int_0^1 g(\tau) d\tau < \infty, \quad (36)$$

i.e., the curve  $\omega$  is of bounded variation.

**Lemma C.5.** If  $\omega \in \text{AC}(X)$ , then

$$\text{Length}(\omega) = \int_0^1 |\omega'|(\tau) d\tau. \quad (37)$$

**Definition C.6 (Length space and geodesic space).** Let  $\omega : [0, 1] \rightarrow X$  be a curve in  $(X, d)$ .

1. The space  $(X, d)$  is a *length space* if

$$d(x, y) = \inf \{ \text{Length}(\omega) : \omega(0) = x, \omega(1) = y, \omega \in \text{AC}(X) \}. \quad (38)$$

2. The space  $(X, d)$  is a *geodesic space* if

$$d(x, y) = \min \{ \text{Length}(\omega) : \omega(0) = x, \omega(1) = y, \omega \in \text{AC}(X) \}. \quad (39)$$

**Definition C.7 (Geodesic).** Let  $(X, d)$  be a length space.

1. A curve  $\omega : [0, 1] \rightarrow X$  is said to be a *constant-speed geodesic* between  $\omega(0)$  and  $\omega(1)$  if

$$d(\omega(t), \omega(s)) = |t - s| \cdot d(\omega(0), \omega(1)), \quad (40)$$

for any  $t, s \in [0, 1]$ .

2. If  $(X, d)$  is further a geodesic space, a curve  $\omega : [0, 1] \rightarrow X$  is said to be a *geodesic* between  $x_0 \in X$  and  $x_1 \in X$  if it minimizes the length among all possible curves such that  $\omega(0) = x_0$  and  $\omega(1) = x_1$ .

Note that in a geodesic space  $(X, d)$ , a constant-speed geodesic is indeed a geodesic. In addition, we have the following equivalent characterization of the geodesic in a geodesic space.

**Lemma C.8.** Let  $(X, d)$  be a geodesic space,  $p > 1$ , and  $\omega : [0, 1] \rightarrow X$  a curve connecting  $x_0$  and  $x_1$ . Then the followings are equivalent.

1.  $\omega$  is a constant-speed geodesic.
2.  $\omega \in \text{AC}(X)$  such that for almost every  $t \in [0, 1]$ , we have

$$|\omega'|(\tau) = d(\omega(0), \omega(1)). \quad (41)$$

3.  $\omega$  solves

$$\min \left\{ \int_0^1 |\tilde{\omega}'|^p dt : \tilde{\omega}(0) = x_0, \tilde{\omega}(1) = x_1 \right\}. \quad (42)$$



## C.2 WASSERSTEIN SPACE

Since the Wasserstein space  $(\mathcal{P}_p(\mathbb{R}^d), W_p)$  for  $p \geq 1$  is a metric space, the following definition specializes Definition C.2 to the Wasserstein metric derivative.

**Definition C.9** (Wasserstein metric derivative). Let  $\{\mu_t\}_{t \in [0,1]}$  be an absolutely continuous curve in the Wasserstein (metric) space  $(\mathcal{P}_p(\mathbb{R}^d), W_p)$ . Then the *metric derivative* at time  $t$  of the curve  $t \mapsto \mu_t$  with respect to  $W_p$  is defined as

$$|\mu'|_p(t) := \lim_{h \rightarrow 0} \frac{W_p(\mu_{t+h}, \mu_t)}{|h|}. \quad (43)$$

For  $p = 2$ , we write  $|\mu'|_p(t) := |\mu'|_2(t)$ .

In the rest of this section, we consider probability measures  $\mu_t$  that are absolutely continuous with respect to the Lebesgue measure on  $\mathbb{R}^d$  and we use  $\mu_t$  denote the probability measure, as well as its density, when the context is clear.

**Theorem C.10.** Let  $p > 1$  and assume  $\Omega \in \mathbb{R}^d$  is compact.

**Part 1.** If  $\{\mu_t\}_{t \in [0,1]}$  is an absolutely continuous curve in  $W_p(\Omega)$ , then for almost every  $t \in [0, 1]$ , there is a velocity vector field  $\mathbf{v}_t \in L^p(\mu_t)$  such that

1.  $\mu_t$  is a weak solution of the continuity equation  $\partial_t \mu_t + \operatorname{div}(\mu_t \mathbf{v}_t) = 0$  in the sense of distributions (cf. the definition in (49) below);
2. for almost every  $t \in [0, 1]$ , we have

$$\|\mathbf{v}_t\|_{L^p(\mu_t)} \leq |\mu'|_p(t), \quad (44)$$

$$\text{where } \|\mathbf{v}_t\|_{L^p(\mu_t)}^p = \int_{\Omega} \|\mathbf{v}_t\|_2^p d\mu_t.$$

**Part 2.** Conversely, if  $\{\mu_t\}_{t \in [0,1]}$  are probability measures in  $\mathcal{P}_p(\Omega)$ , and for each  $t \in [0, 1]$  we suppose  $\mathbf{v}_t \in L^p(\mu_t)$  and  $\int_0^1 \|\mathbf{v}_t\|_{L^p(\mu_t)} dt < \infty$  such that  $(\mu_t, \mathbf{v}_t)$  solves the continuity equation, then we have

1.  $\{\mu_t\}_{t \in [0,1]}$  is an absolutely continuous curve in  $(\mathcal{P}_p(\mathbb{R}^d), W_p)$ ;
2. for almost every  $t \in [0, 1]$ ,

$$|\mu'|_p(t) \leq \|\mathbf{v}_t\|_{L^p(\mu_t)}. \quad (45)$$

As an immediate corollary, we have the following dynamical representation of the Wasserstein metric derivative.

**Corollary C.11.** If  $\{\mu_t\}_{t \in [0,1]}$  is an absolutely continuous curve in  $(\mathcal{P}_p(\mathbb{R}^d), W_p)$ , then the velocity vector field  $\mathbf{v}_t$  given in Part 1 of Theorem C.10 must satisfy

$$\|\mathbf{v}_t\|_{L^p(\mu_t)} = |\mu'|_p(t). \quad (46)$$

Corollary C.11 suggests that  $\mathbf{v}_t$  can be viewed as the *tangent vector field* of the curve  $\{\mu_t\}_{t \in [0,1]}$  at time point  $t$ . Moreover, Corollary C.11 suggests the following (Euclidean) gradient flow for tracking particles in  $\mathbb{R}^d$ : let  $y(t) := y_x(t)$  be the trajectory starting from  $x \in \mathbb{R}^d$  (i.e.,  $y(0) = x$ ) that evolves according the ordinary differential equation (ODE)

$$\frac{d}{dt} y(t) = \mathbf{v}_t(y(t)). \quad (47)$$

The dynamical system (47) defines a flow  $Y_t : \Omega \rightarrow \Omega$  of vector field  $\mathbf{v}_t$  on  $\Omega$  via

$$Y_t(x) = y(t). \quad (48)$$

Then, it is straightforward to check that the pushforward measure flow  $\mu_t := (Y_t)_\# \mu_0$  and the chosen velocity vector field  $\mathbf{v}_t$  in the ODE (47) is a weak solution of the continuity equation  $\partial_t \mu_t + \operatorname{div}(\mu_t \mathbf{v}_t) = 0$  in the sense that

$$\frac{d}{dt} \int_{\Omega} \phi dt = \int_{\Omega} \langle \nabla \phi, \mathbf{v}_t \rangle d\mu_t, \quad (49)$$

for any  $\mathcal{C}^1$  function  $\phi : \Omega \rightarrow \mathbb{R}$  with compact support.

*Theorem C.12 (Constant-speed Wasserstein geodesic).* Let  $\Omega \in \mathbb{R}^d$  be a convex subset and  $\mu, \nu \in \mathcal{P}_p(\Omega)$  for some  $p > 1$ . Let  $\gamma$  be an optimal transport plan under the cost function  $\|x - y\|_p^p$ . Define

$$\begin{aligned}\pi_t &: \Omega \times \Omega \rightarrow \Omega, \\ \pi_t(x, y) &= (1 - t)x + ty,\end{aligned}$$

as the linear interpolation between  $x$  and  $y$  in  $\Omega$ . Then, the curve  $\mu_t = (\pi_t)_\# \gamma$  is a constant-speed geodesic in  $(\mathcal{P}_p(\mathbb{R}^d), W_p)$  connecting  $\mu_0 = \mu$  and  $\mu_1 = \nu$ .

If  $\mu$  has a density with respect to the Lebesgue measure on  $\mathbb{R}^d$ , then there is an optimal transport map  $T$  from  $\mu$  to  $\nu$  (Brenier, 1991). According to Theorem C.12, we obtain *McCann's interpolation* (McCann, 1997) in the Wasserstein space as

$$\mu_t = [(1 - t)\text{id} + tT]_\# \mu, \quad (50)$$

which is a constant-speed geodesic in  $(\mathcal{P}_p(\mathbb{R}^d), W_p)$ .  $\text{id}$  is the identity function in  $\mathbb{R}^d$ .

To sum up, we collect the following facts about the geodesic structure and dynamical formulation of the OT problem. Let  $p > 1$ , and  $\Omega \subset \mathbb{R}^d$  be a convex subset (either compact or have no mass escaping at infinity).

1. The metric space  $(\mathcal{P}_p(\Omega), W_p)$  is a geodesic space.
2. For  $\mu, \nu \in \mathcal{P}_p(\Omega)$ , a constant-speed geodesic  $\{\mu_t\}_{t \in [0,1]}$  in  $(\mathcal{P}_p(\Omega), W_p)$  between  $\mu$  and  $\nu$  (i.e.,  $\mu_0 = \mu$  and  $\mu_1 = \nu$ ) must satisfy  $\mu_t \in \text{AC}(\mathcal{P}_p(\Omega))$  and

$$|\mu'|_p(t) = W_p(\mu(0), \mu(1)) = W_p(\mu, \nu) \quad (51)$$

for almost every  $t \in [0, 1]$ .

3. The above  $\mu_t$  solves

$$\min \left\{ \int_0^1 |\tilde{\mu}'|^p(t) dt : \tilde{\mu}(0) = \mu, \tilde{\mu}(1) = \nu, \tilde{\mu} \in \text{AC}(\mathcal{P}_p(\Omega)) \right\}. \quad (52)$$

4. The above  $\mu_t$  solves the Benamou-Brenier problem

$$W_p^p(\mu, \nu) = \min \left\{ \int_0^1 \|\mathbf{v}_t\|_{L^p(\tilde{\mu}_t)}^p dt : \tilde{\mu}(0) = \mu, \tilde{\mu}(1) = \nu, \partial_t \tilde{\mu}_t + \text{div}(\tilde{\mu}_t \mathbf{v}_t) = 0 \right\}, \quad (53)$$

and  $\mu_t = \mu(\cdot, t)$  defines a constant-speed geodesic in  $(\mathcal{P}_p(\Omega), W_p)$ .

## D ENTROPIC REGULARIZATION

Our GeONet is compatible with entropic regularization, which is closely related to the Schrödinger bridge problem and stochastic control (Chen et al., 2016). Specifically, the entropic-regularized GeONet (ER-GeONet) solves the following fluid dynamic problem:

$$\begin{aligned} \min_{(\mu, \mathbf{v})} & \int_0^1 \int_{\mathbb{R}^d} \frac{1}{2} \|\mathbf{v}(x, t)\|_2^2 \mu(x, t) dx dt \\ \text{subject to} & \partial_t \mu + \text{div}(\mu \mathbf{v}) + \varepsilon \Delta \mu = 0, \quad \mu(\cdot, 0) = \mu_0, \quad \mu(\cdot, 1) = \mu_1. \end{aligned} \quad (54)$$

Applying the same variational analysis as in the unregularized case  $\varepsilon = 0$  (cf. Appendix B), we obtain the KKT conditions for the optimization (54) as the solution to the following system of PDEs:

$$\partial_t \mu + \text{div}(\mu \nabla u) = -\varepsilon \Delta \mu, \quad (55)$$

$$\partial_t u + \frac{1}{2} \|\nabla u\|_2^2 = \varepsilon \Delta u, \quad (56)$$

with the boundary conditions  $\mu(\cdot, 0) = \mu_0, \mu(\cdot, 1) = \mu_1$  for  $\varepsilon > 0$ . Note that (56) is a parabolic PDE, which has a unique smooth solution  $u^\varepsilon$ . The term  $\varepsilon \Delta u$  effectively regularizes the (dual) Hamilton-Jacobi equation in (7). In the zero-noise limit as  $\varepsilon \downarrow 0$ , the solution of the optimal entropic interpolating flow (54) converges to solution of the Benamou-Brenier problem (4) in the sense of the method of vanishing viscosity (Mikami, 2004; Evans, 2010).

## E GRADIENT ENHANCEMENT

In practice, we may fortify the base method by adding extra residual terms of the differentiated PDEs to our loss function of GeONet. Such gradient enhancement technique has been used to strengthen PINNs (Yu et al., 2022), which improves efficiency as fewer data points are needed to be sampled from  $U(\Omega) \times U(0, 1)$ , and prediction accuracy as well.

The motivation behind gradient enhancement stems minimizing the residual of a differentiated PDE. We turn our attention to PDEs of the form

$$\begin{cases} \mathcal{F}(x, t, \partial_{x_1} u, \dots, \partial_{x_d} u, \partial_{x_1 x_1} u, \dots, \partial_{x_d x_d} u, \dots, \partial_t u, \lambda) = 0 & \text{on } \Omega \times [0, 1], \\ u(\cdot, 0) = u_0, \quad u(\cdot, 1) = u_1 & \text{on } \Omega, \end{cases} \quad (57)$$

for domain  $\Omega \subseteq \mathbb{R}^d$ , parameter vector  $\lambda$ , and boundary conditions  $u_0, u_1$ . One may differentiate the PDE function  $\mathcal{F}$  with respect to any spatial component to achieve

$$\frac{\partial}{\partial x_\ell} \mathcal{F}(x, t, \partial_{x_1} u, \dots, \partial_{x_d} u, \partial_{x_1 x_1} u, \dots, \partial_{x_d x_d} u, \dots, \partial_t u, \lambda) = 0. \quad (58)$$

The differentiated PDE is additionally equal to 0, similar to what we see in a PINN setup. If we substitute a neural network into the differentiated PDE of (58), what remains is a new residual, just as we saw with the neural network substituted into the original PDE. Minimizing this new residual in the related loss function characterizes the gradient enhancement method.

We utilize the same loss function in (14), but we add the additional terms

$$\mathcal{L}_{\text{GE,cty},i} = \frac{1}{N} \sum_{\ell=1}^d \gamma_\ell \left\| \frac{\partial}{\partial x_\ell} \left( \frac{\partial}{\partial t} \mathcal{C}_{\phi,i} + \text{div}(\mathcal{C}_{\phi,i} \nabla \mathcal{H}_{\psi,i}) \right) \right\|_{L^2(\Omega \times (0,1))}^2, \quad (59)$$

$$\mathcal{L}_{\text{GE,HJ},i} = \frac{1}{N} \sum_{\ell=1}^d \omega_\ell \left\| \frac{\partial}{\partial x_\ell} \left( \frac{\partial}{\partial t} \mathcal{H}_{\psi,i} + \frac{1}{2} \|\nabla \mathcal{H}_{\psi,i}\|_2^2 \right) \right\|_{L^2(\Omega \times (0,1))}^2, \quad (60)$$

where the variables and neural networks that also appeared in (14) are the same. Here  $\gamma_\ell$  and  $\omega_\ell$  are positive weights. The summation is taken in order to account for gradient enhancement of each spatial component of  $x \in \Omega$ .

## F DEEPONETS

A challenge resides in solving the risk minimization problem over numerous instances of data. This challenge may be conciliated by instituting a DeepONet that learns a general nonlinear operator, where one (or a pair of) neural network(s) encode(s) the input and another encodes the collocation samples. This architecture originates as an equivalence to the universal approximation theorem for operators.

**General DeepONet.** A general operator  $G^\dagger$  may be approximated by an unstacked DeepONet (Chen and Chen, 1995; Lu et al., 2021)

$$G^\dagger(u_0)(x, t) \approx \sum_{k=1}^p \mathcal{B}_k(u_0(x_1), \dots, u_0(x_m), \theta) \cdot \mathcal{T}_k(x, t, \xi), \quad (61)$$

where  $\mathcal{B}_k, \mathcal{T}_k$  are scalar elements of output of neural networks  $\mathcal{B}, \mathcal{T}$ , and  $p$  is a constant denoting the number of such elements. We take  $\mathcal{B}$  and  $\mathcal{T}$  to be artificial neural networks parameterized by  $\theta, \xi$  respectively.  $\mathcal{B}, \mathcal{T}$  are known as the branch and trunk networks respectively.  $u_0$  is the initial function in which the operator is applied, evaluated at distinct locations  $x_1, \dots, x_m$  for branch input.  $(x, t)$  is any arbitrary point in space and time in which  $G^\dagger(u_0)$  may be evaluated.

**Enhanced DeepONet.** The above framework is restricted to one initial input function  $u_0$ . We turn our attention to the enhanced DeepONet, a DeepONet styled to act upon dual initial conditions Tan and Chen (2022). Our true operator  $\Gamma^\dagger$  may be approximated using a second neural network encoder for input  $u_1$ ,

---


$$\Gamma^\dagger(u_0, u_1)(x, t) \approx \sum_{k=1}^P \mathcal{B}_k^0(u_0(x_1), \dots, u_0(x_m), \theta^0) \cdot \mathcal{B}_k^1(u_1(x_1), \dots, u_1(x_m), \theta^1) \cdot \mathcal{T}_k(x, t, \xi). \quad (62)$$

**Physics-informed DeepONet.** The enhanced DeepONet may be substituted into any physics-informed framework, such as that of equation (9), taking place of the PDE solution value in the empirical loss to be minimized Wang et al. (2021). Generalization of the trained DeepONet permits any solution to the PDEs to be evaluated instantaneously given the appropriate input function(s).

## G MODIFIED MULTI-LAYER PERCEPTRON

Here we outline the forward pass of the modified multi-layer perceptron used throughout the bivariate and MNIST encoder experiments. Let  $\sigma$  denote an activation function (typically tanh),  $X$  as neural network design input,  $W^i$  the weights of the neural network at index  $i$ , and  $b^i$  the bias at index  $i$ . Here,  $X$  can refer to either branch or trunk inputs, as this architecture is used for both.

The forward pass is given by

$$U = \sigma(W^1 X + b^1), \quad V = \sigma(W^2 X + b^2) \quad (63)$$

$$H^1 = \sigma(W^{h,1} X + b^{h,1}) \quad (64)$$

$$Z^k = \sigma(W^{z,k} H^k + b^{z,k}) \quad (65)$$

$$H^k = (1 - Z^{k-1}) \odot U + Z^{k-1} \odot U \quad (66)$$

$$\mathcal{N}_\theta = W^\ell H^\ell + b^\ell, \quad (67)$$

where  $k \in \{1, \dots, \ell\}$ ,  $\odot$  is an element-wise product, and  $\mathcal{N}_\theta$  is the neural network final output, either a branch or a trunk.

---

## H HYPERPARAMETER SETTINGS AND TRAINING DETAILS

We discuss training characteristics of GeONet based on the primary experiments. An unmodified Adam optimizer was chosen for all branch, trunk neural networks with a learning rate starting from  $5e-4$ . All layers share the same width. We use tanh activation for all neural networks. Coefficients  $\alpha_1, \alpha_2, \beta_0, \beta_1$  were computed after examining errors. Coefficients were selected in the range  $[0.05, 20]$ . Neural network depths refer to  $\ell$  in each modified MLP. Training is done on a NVIDIA T4 GPU.

Table 4: Architecture and training details in our experimental Section 4 and Appendix I.

Hyperparameter	1D Gaussians	2D Gaussians	Encoded MNIST
No. of initial conditions $(\mu_0, \mu_1)$	20,000	5,000	5,000
$m$ (branch input dimension)	100	576	32
Branch width	150	200	150
Branch depth	7	7	7
Trunk width	100	150	100
Trunk depth	7	7	7
$p$ (dimension of outputs)	800	800	200
Batch size	2,000	2,000	1,000
Final training time	$\sim 2$ hrs	$\sim 2$ hrs	$\sim 4$ hrs
Final training loss	$\sim 1.5e-4$	$\sim 1.8e-5$	$\sim 2.0e-2$
$\alpha_1, \alpha_2, \beta_0, \beta_1$	0.5, 0.25, 1, 1	0.5, 0.25, 1, 1	1, 1, 1, 1

---

## I TRAINING AND PERFORMANCE

### I.1 UNIVARIATE AND BIVARIATE GAUSSIAN MIXTURE EXPERIMENTS

**Univariate Gaussians.** We choose spatial domain  $x \in \Omega = [0, 10]$  discretized into a 100 point mesh. We generate 20,000 training pairs  $(\mu_0, \mu_1)$  of Gaussians, taking  $k_j = 6$  for the number of Gaussians in each mixture. We take means  $\mu_i \in [2, 8]$  and variances  $\Sigma_i \in [0.5, 0.6]$  uniformly. Empirically, we found a large batch size more suitable for training than a low one, and so we take a batch size of 2,000, meaning this many uniform collocation points are taken for both the PDE residuals and boundary points for each training iteration. We choose physical loss coefficient  $\alpha_1 = 0.5, \alpha_2 = 0.25$ , with boundary coefficients  $\beta_0 = \beta_1 = 1$ . We found these coefficients a good balance to enforce the physical constraint without sacrificing boundary restrictions after iterating these coefficients among  $[0.05, 20]$  and examining error. Additional training details are given in Appendix H.

**Bivariate Gaussians.** In our experiment, domain  $\Omega = [0, 5] \times [0, 5] \subseteq \mathbb{R}^2$  was chosen, which was discretized into a  $24 \times 24$  grid for GeONet input, meaning the branch networks took vector input of 576 in length for each. We generate 5,000 training pairs  $(\mu_0, \mu_1)$ . Recall that GeONet is mesh-invariant, so the  $24 \times 24$  grids can be adapted to any higher resolution, which is used in figure 4. We use a combination of low and high variance Gaussians in the mixture, 6 of which had variance in  $[0.35, 0.4]$  and 6 in  $[0.75, 0.9]$ , giving a total of 12 Gaussians in each mixture in each pair. Covariance was in  $[-0.1, 0.1]$ . Additional training details are given in Appendix H.

**Training.** To compute the DeepONet derivatives, we take the inner product in the enhanced DeepONet as in equations (12), (13), and subsequently use automatic differentiation after the inner products are taken. Alternatively, one may compute a Hessian for the second-order derivatives, but this is costly in terms of memory, meaning a large batch size cannot be used without a monumental memory cost. We found the neural networks do not train properly without a large batch size, and so this method of differentiation is not viable. We found the DeepONet output dimension taken to be quite large slightly outperforms a lower-dimension output given sufficient data and no overfitting. In the univariate Gaussian experiment, we take  $p = 800$ , which outperformed  $p = 200$  by reducing training loss from approximately  $2.5\text{e-}4$  to  $1.5\text{e-}4$  and reducing test error by about 1%. In the bivariate experiment, changing  $p = 400$  to  $p = 800$  reduced training loss from approximately  $2.1\text{e-}5$  to  $1.8\text{e-}5$ . Architecture generally made some difference to training loss, but not significant, making a width of around 100-200 suitable for branches and trunks. For example, increasing branch width in the univariate experiment from 100 to 150 lowered training loss by approximately  $4\text{e-}5$ . Increasing branch width to 200 and trunk width to 150 from 150 and 100 respectively had minimal effect, lowering training loss by about  $1\text{e-}5$ . We found the modified MLP architecture preferable, lowering final training loss from approximately  $3\text{e-}4$  with standard architecture for univariate Gaussians.

**Performance.** Our baseline results were collected by probing GeONet on the identity geodesic in Table 2. The baseline identity geodesic provides a benchmark for comparing and interpreting the errors across different setups. From Table 2, we can draw the following observations. The loss boundary conditions (17) allow greater precision for  $t = 0, 1$ , which suggests that lack of data-enforced conditions along the inner region of the time continuum would cause greater error. Errors for predicting the univariate Gaussian trivial identity geodesic in the intermediate  $t = 0.25, 0.5, 0.75$  are uniformly smaller than other in-distribution setups since the former is an easier task. In the bivariate experiment, we found that error quickly rises as variance decreases, which is equivalent to a task of learning more complicated geodesics. We did not find lower variance drastically affects performance in the univariate experiment, suggesting GeONet and potentially physics-informed DeepONets in general are less effective as dimension increases. We did not find the number of Gaussians in the mixtures drastically affected results, but naturally more complicated geodesics induce greater error, which is to be expected. We found bivariate errors are similar to the random case as in the identity case, suggesting there is some notion of base neural operator error, which may not exist with simpler data.

### I.2 MNIST EXPERIMENT

**Training.** To learn the geodesic, we ensure all values within the encoded representation are nonnegative, meaning we can shift all encoded representations by some arbitrary constant. We choose 10 for this. This constant can be deducted in later stages to ensure the valid representation is met. A domain

of  $[0, 5]$  was divided into an equispaced mesh of 32 points for the encoded representation. This domain is rather arbitrary and is chosen simply for DeepONet input purposes, which can be modified as seen fit. 5,000 encoded pairs were chosen to train GeONet, but the pretrained autoencoder was done on the entirety of MNIST with a batch size of 500 and 120 iterations per epoch. Additional training details are found in Appendix H.

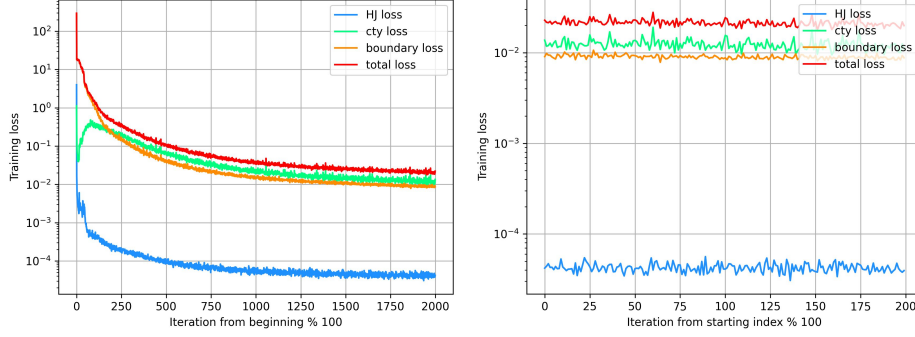


Figure 8: We examine iterations of the Adam optimizer in the total and late training on a log scale. The learning rate was modified every iteration. We examine late training in order to observe oscillatory behavior between the continuity and Hamilton-Jacobi loss to see if they adversarially compete in late training. We do not observe this pattern, and the continuity loss greatly surpasses the HJ loss in value. These graphs were created using the encoded MNIST experiment.

**Performance.** GeONet performs well in this experiment. Scaling the physics-informed term by a constant less than one did not prove necessary in this experiment to ensure all loss terms are met to a sufficient degree. As before, boundary terms are uniformly smaller, likely since these terms are known and included in the loss function to be minimized. The same error metric is used as in the synthetic experiments but with normalization, making the  $L^1$  error relative. We remark OOD generalization is omitted because the distribution of the encoded data is not known. We also remark the decoded images, being the geodesic returned to its original state, do not directly translate to a geodesic performed upon an original pair of images. NaN values are omitted in the error computations, which are possible in the POT solutions due to the irregularity of the initial conditions.

**Regularization.** Classical geodesic algorithms require a small regularization parameter in order to be computed. This provides affects the synthetic experiments trivially, but we found this regularization induces greater in the MNIST experiment. This is to be considered when evaluating the errors, and true error is likely smaller between GeONet and the reference geodesics computed with POT than what is displayed. This regularization acts as a form of "smoothing" of the solutions.

### I.3 OUT-OF-DISTRIBUTION GENERALIZATION.

To examine the generalization performance of GeONet under distribution shifts, we consider a setup which is out-of-distribution (OOD) at test time. To do this, we alter the variances to be lower than in the training setup. Changing the number of Gaussians in the mixture at test time does not yield a significant enough of an alteration to the experiment. For univariate Gaussians, variance was among  $[0.3, 0.4]$  instead of the  $[0.5, 0.6]$  in training. For bivariate Gaussians, we take variances in  $[0.25, 0.3]$  and  $[0.65, 0.8]$ , six of each in each mixture. Empirically, we found OOD generalization had lower error in this experiment than in the univariate case, which may be because the support of areas of low variance have relatively low measure. This bivariate error does indeed scale greater as variance decreases even more. We remark the lower variance generally yields a more sophisticated task in learning the geodesic, and error even trained upon such data is higher than with high variance.

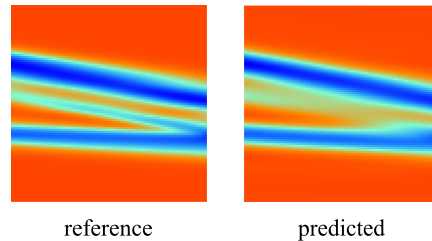


Figure 9: An illustration of an OOD univariate Gaussian mixture geodesic at test time.



---

## J SAMPLE HJ GRAPHS

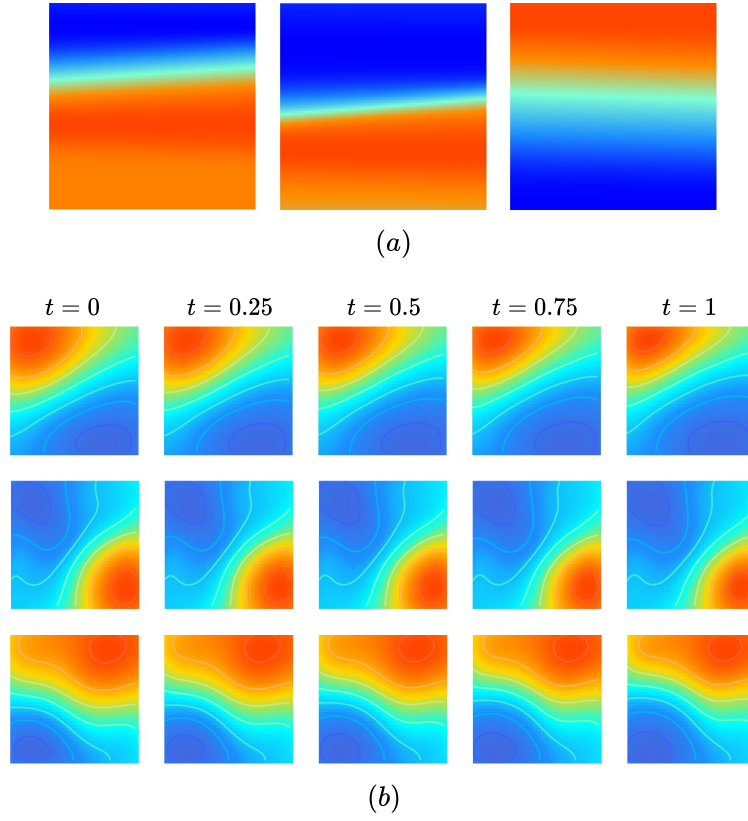


Figure 10: We present sample HJ equations for (a) three univariate Gaussian mixtures and (b) three bivariate Gaussian mixtures from the primary experiments performed in Section 4. The univariate HJ samples at certain times are the vertical cross sections of the graphs, and the bivariate samples are given at certain times.